1996 ASME International Mechanical Engineering Congress and Exposition, Atlanta, Nov 1996, DSC-Vol. 58 pp. 483-488

DESIGN OF A HEMISPHERICAL MAGNETIC LEVITATION HAPTIC INTERFACE DEVICE

Peter J. Berkelman, Zack J. Butler, and Ralph L. Hollis
The Robotics Institute
Carnegie Mellon University
Pittsburgh, PA 15213

ABSTRACT

We are currently fabricating a haptic interface device to enable direct physical interaction with dynamic simulated three-dimensional environments by exerting and reacting to forces and motions between the user's hand and a magnetically levitated object. Our device uses magnetic levitation rather than a motorized linkage so that the dynamics are simple and actuator nonlinearities such as hysteresis, backlash and static friction are eliminated. Magnetic levitation haptic interaction was previously demonstrated using a fine motion robot wrist. A new magnetic levitation device was then designed specifically to address the requirements of realistic tool-based haptic interaction. A hemispherical device shape was adopted to maximize the ranges of translation and rotation and the ratio of actuator surface area to the levitated mass while enabling the user to grip a tool handle at the hemisphere center, near the center of mass, where translation, rotation, force, and torque ranges are the same in all directions. The new device will have a motion range of at least ± 12 mm and $\pm 7°$, position sensing resolution within 3 μm, and will be capable of generating peak forces up to 60 N. Preliminary results from testing of position sensors and actuator assemblies support the performance data obtained from model analysis.

1 INTRODUCTION

To provide realistic interaction between the user and the simulated environment, a haptic interface device must accurately reproduce the dynamic behavior of the simulated environment and be easy and natural for the user to manipulate. The important characteristics of the interface device are its force and motion ranges, motion resolution, control bandwidths, and ease of use.

Early examples of haptic interface devices were generally backdriven serial robot manipulators that had disadvantages of mechanical friction and backlash, low bandwidth, and large bulk and weight as well as being difficult and tiring to use [1]. Much better performance has been obtained with parallel actuated devices using tensioned cables and/or lightweight, smooth mechanical linkages [2, 3]. An especially successful example of this type of device is the "PHANToM" from SensAble Devices, Inc [4]. The PHANToM is limited to only three degrees of freedom, however, so that its dynamic impedance is generated for a single point in space rather than for a rigid body.

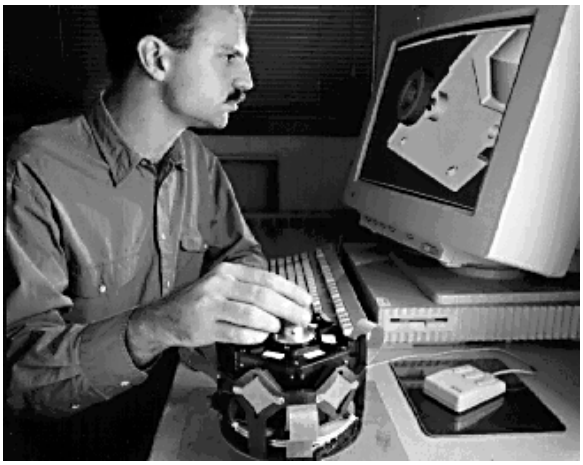

Figure 1: Using a Desktop Maglev Haptic Interface Device

The Lorentz force has been proposed as a superior actuation means for haptic interface devices [5]. Lorentz force actuation is generated by electric currents in a magnetic field. This method of non-contact actuation is simple and compact. It enables high control bandwidths and resolutions while eliminating many shortcomings of motor drives and linkages such as friction, hysteresis, and backlash. A single moving part can be controlled in all six degrees of

freedom.

With an appropriate configuration of magnet assemblies on the base or "stator" and flat coils embedded in the levitated object or "flotor," the flotor can be levitated and controlled to exhibit any dynamic rigid-body behavior within the limitations of its control bandwidth and ranges of force and motion. The position sensing necessary for feedback control can be done optically using LEDs and position-sensing photodiodes. The characteristic features of a magnetic levitation haptic interface are high control bandwidth due to non-contact actuation, simple dynamics and low inertia for the levitated object, and compact size which allows the device to be used on a desktop with a workstation and graphical display. An example of using a fully integrated interaction system is shown in Fig. 1.

The haptic interaction provided by the device is tool-based: As it is manipulated by the user, the handle on the flotor is represented in the dynamic simulation by a given rigid hand tool which is meaningful in the context of the given application. The user can then feel any physical interaction affecting that tool. For example, a haptic CAD assembly system could represent the flotor as a screwdriver or wrench through which the user feels impacts, texture, and friction. A surgical simulation system could represent the tool as a scalpel through which the user feels the resistance of bone, muscle, and connective tissue.

2 PREVIOUS DEMONSTRATION DEVICE

Previously, a fine motion robot wrist using magnetic levitation was adapted in our laboratory for use as a haptic interface with simple simulated dynamic environments such as slider and rotor mechanisms, hard polygonal contacts, dry and viscous friction, and textured surfaces [6]. This device has a position bandwidth of over 50 Hz with a 1000 Hz control cycle and position resolution high enough to enable surprisingly realistic haptic interaction involving hard polygonal contacts, friction, and surface texture. The robot wrist is controlled by a realtime VMEbus system with a digital signal processor communicating via Ethernet TCP/IP sockets with a graphical user interface on a host workstation.

The effectiveness of the robot wrist is limited, however, by its small motion range and awkwardness in operation. The maximum displacement of the flotor is either ± 5 mm in translation or $\pm 3.5°$ in rotation in any direction. The hexagonal box shape of the flotor results in restricted translation towards the edge of its rotation range (and vice versa), since the corners of the flotor collide with the actuator magnets on the stator.

The ball handle grasped by the user is mounted on top of the flotor several cm from its center (as shown in Fig. 2), but users generally feel more comfortable grasping the main body of the flotor rather than the ball grip. The flotor would be easier to manipulate if the handle were nearer to the centers of mass and actuation of the flotor; also haptic interaction would be more effective if the center of the maximum possible rotation were near the handle.

To reduce these described limitations in motion, forces, bandwidth, and ease of use, a new hemispherical device specifically designed for haptic interaction is being made.

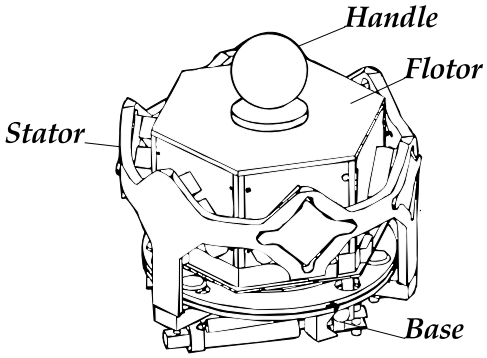

Figure 2: Previously Developed Maglev Robot Wrist Used as a Haptic Interface

3 HEMISPHERICAL MAGNETIC LEVITATION HAPTIC INTERFACE DEVICE

The design goals for the new device are (1) to increase the range of motion to at least ± 12 mm and $\pm 7°$ of rotation in all directions, (2) to have a position resolution of approximately 3 μm or less, (3) to enable a variety of tool handles to be mounted at the flotor center with an optional force-torque sensor so that it can be easily grasped and manipulated by the user, and (4) to have a position bandwidth as high as possible, at least as high as the current robot wrist haptic device. The increased range of motion of the device more closely corresponds to a comfortable range of fingertip motions while the user's wrist is supported on a flat surface.

The body of the flotor for the new device is a hemispherical shell. The curved shape of the flotor results in independent ranges of rotation and translation, allows an equal range of motion in all directions, and enables the user to easily grasp a handle located at the center. The stator completely encloses the flotor except for an inner hole through which the handle support rod projects, an outer hole where all necessary wiring from the flotor will hang down, and additional holes for cooling air circulation.

The entire device will be embedded in a desktop so that the handle gripped by the user and the top rim of the stator hemisphere are approximately level with the desktop surface when the flotor is in the center position. This configuration allows the user's wrist and forearm to rest on the stator rim and desktop while the haptic device tool handle is manipulated with the fingertips. This position results in more comfortable and natural manipulation as well as more sensitive fingertip control for the user since the weight of the hand is supported by and braced against the stator rim. The typical position of the user's hand as the haptic device is operated is shown in Fig. 3.

As the device is manipulated by the user, the control and simulation systems cause the flotor dynamics to reproduce the calculated dynamics in real time of a virtual tool in the given simulated task, for example CAD assembly using a screwdriver as shown in Fig. 4. The reaction dynamics on the tool are felt by the user through the fingertips.

The hemispherical device shape poses challenges in part design and fabrication, since the internal parts of the hap-

Figure 3: Operation of the New Haptic Device

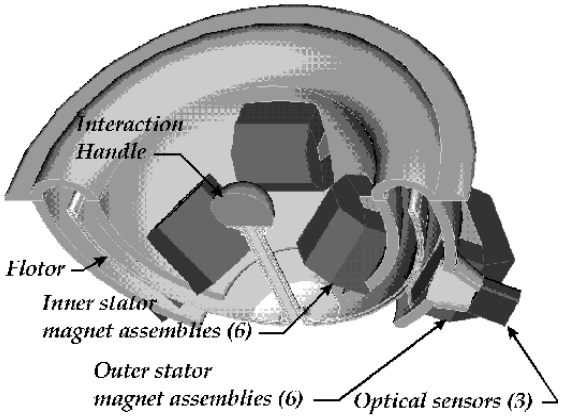

Figure 5: Cutaway View of the Haptic Device

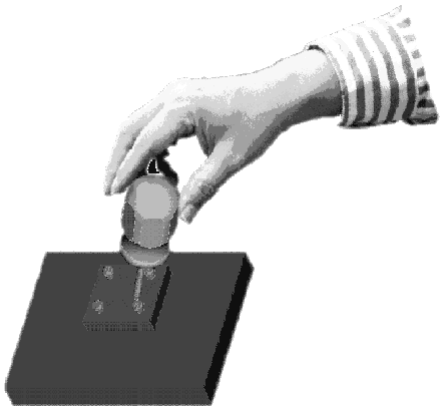

Figure 4: Example Haptic Task Emulated by Device

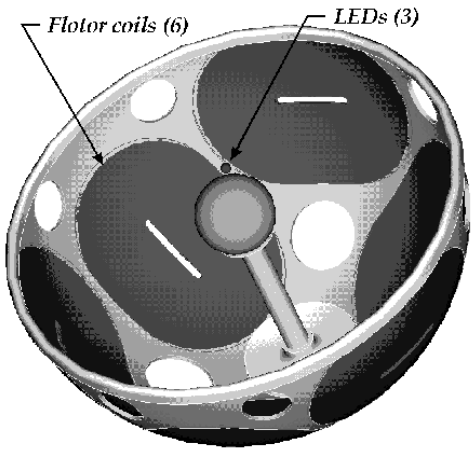

Figure 6: Flotor with Coil and LED Placement

tic device must conform to the given curvature. To conform to this new hemispherical geometry and the increased range of motion, the actuator configuration, magnet assemblies, and the position sensing system had to be completely redesigned for the new device. Figure 5 shows a cutaway representation of the device showing the principal parts including the levitated flotor, the stator enclosure, magnet and sensor assemblies, and the tool handle.

The flotor must have a minimum levitated mass yet high stiffness, so it is designed with as few parts as possible. The main body of the flotor is a hemispherical thin aluminum shell with large oval cutouts for the actuator coils. The coils fit closely together to maximize the area on the flotor used to generate actuation forces. LEDs for position sensing fit snugly between the coils. The coils are wound from ribbon wire on spherical forms to fit the curvature of the flotor. Either aluminum wire can be used to minimize the levitated mass, or copper to minimize electrical resistance and the heat generated thereby. Two additional very thin shells are bonded to the main shell to enclose the coils and provide eddy current damping as the flotor moves through the stationary magnetic fields. The shells are spun from aluminum sheet and bonded together with vibration-damping adhesive from 3M. A machined ring is fastened to the upper rim of the hemisphere shells to increase stiffness. The tool handle for user manipulation is mounted at the center of the aluminum shells. A miniature force sensor can be mounted between the tool handle and the flotor shell stem for precise force control or inertial compensation. The flotor assembly is shown in Fig. 6.

The inner and outer stator shells are machined from near-net-shape hemispherical shell castings with cutouts and flats to house the magnet and position sensor assemblies. The shells must be thick enough to withstand the stresses caused by the attraction between the inner and outer magnet assemblies. A horizontal circular flange extends from the rim of the stator so it can be easily mounted to the desktop.

4 ACTUATION

To efficiently generate forces and torques in all directions, the actuators are arranged in a tightly-packed configuration equally spaced around the circumference of the flotor with three actuators immediately below the rim and the other three centered 45° below the rim. Each oval-shaped actuator coil is curved to conform to the flotor shell and spans a $45° \times 61°$ solid angle on the hemisphere. The six oval-shaped flat actuator coils together occupy approximately two-thirds of the flotor area. The flotor shell radius of 115 mm is a tradeoff to allow large actuator surface areas and forces, yet minimize the mass to be levitated.

Curved coils are less effective than flat coils of the same area for generating forces, since not all of the force is generated in the same direction. They are equally effective at generating torques, however, since all points on the coil are equidistant from the flotor center.

The forces and torques generated on the flotor when it is in the centered position can be expressed as $\mathbf{F} = \mathbf{AI}$, where $\mathbf{F}$ is a 6-vector consisting of the forces and torques exterted on the flotor center, $\mathbf{I}$ a 6-vector of the coil currents, and $\mathbf{A}$ the matrix which maps them. $\mathbf{A}$ can be calculated from the sums of the Lorentz forces and torques

$$f_i = I_i \times B_i,$$

$$\tau_i = c_i \times f_i,$$

where B_i are the magnetic fields of each magnet assembly air gap and c_i are the coil center locations [7].

With a normalized unit flotor radius and magnetic fields, the actuator configuration described above results in the transform matrix:

$$\mathbf{A} = \begin{bmatrix} 0 & 0.191 & 0.866 & -0.383 & -0.866 & 0.191 \\ -1.000 & 0.331 & 0.500 & 0 & 0.500 & -0.331 \\ 0 & -0.924 & 0 & -0.924 & 0 & -0.924 \\ 0.707 & -0.866 & -0.354 & 0 & -0.354 & 0.866 \\ 0 & 0.500 & 0.612 & -1.000 & -0.612 & 0.500 \\ -0.707 & 0 & -0.707 & 0 & -0.707 & 0 \end{bmatrix}$$

The distribution of the singular values of this matrix indicates the effectiveness of the actuator configuration in generating forces and torques in different directions. A singular value decomposition on $\mathbf{A}$ yields a vector of singular values from largest to smallest:

$$\mathbf{s} = [1.908 \;\; 1.908 \;\; 1.600 \;\; 1.225 \;\; 0.573 \;\; 0.573]^T.$$

Due to rotational symmetry, this configuration must generate forces and torques in the two horizontal axes equally effectively.

Therefore, this singular value decomposition indicates that this actuator configuration is somewhat less effective at generating vertical forces compared to the horizontal, yet approximately twice as effective at generating torques about the vertical axis than the horizontals. Intuitively, it can be seen that the device must generate forces less effectively in the vertical direction, since no actuator alone can generate a purely vertical force. The actuation force currents necessary to counteract the flotor weight in gravity are equally distributed over the three rim coils to prevent the coils overheating.

Magnet assembly design was carried out using a field simulator finite element (FEA) analysis software package. A full three-dimensional FEA model was used rather than a simplified 2D one due to the high energy product of the permanent magnets and the large size of the air gap relative to the size of the magnets. The air gap between the inner and outer magnet assemblies is 32 mm to accomodate the thickness of the flotor, its range of motion, and its curvature. The magnet sizes are $20 \times 50 \times 25$ mm, to provide a field strength of 0.35 T at the center of the air gap using a minimum amount of 48 MGOe NdFeB permanent magnet material. The separation distance and angle between the two pairs of magnets in each assembly was determined by the size of the actuator coils and the range of motion of the flotor. A current of 2 A through each of the three rim coils when the flotor is in the center positon is predicted to result in 60 N of vertical force. The flotor mass is predicted to be 1.5 Kg or less.

Because of the large air gap in each magnet assembly, the magnetic field varies from 0.2 T at the edge of the gap, to 0.35 T at the center, to 0.6 T by the faces of the magnets. Due to this variation, the Lorentz force obtained from the coil current is dependent on the position of the coil in the air gap: The force will increase as the coil approaches the faces of the magnets and decrease as it moves sideways so that less of the coil is exposed to the areas of high magnetic field. This force variation can be compensated either through a lookup table indexed by the displacement of the coil in the two directions described, or by utilizing a force sensor in the handle of the flotor to close a feedback loop on the desired forces to be exerted.

Currently, one set of magnets has been assembled; the peak measured field strength agrees with data from the finite element analysis to within 4%. The FEA result showing the magnetic field in the plane in the center of the air gap is given in Fig. 7, while the measured magnetic field from the fabricated assembly is shown in Fig. 8. The contour lines in each plot correspond to B-field magnitudes from 0.15 T to 0.325 T in steps of 0.025 T. Errors in the FEA derive from the quantization in the finite element mesh; errors in measurement are from limited positioning accuracy and resolution due to the 4 mm width of the gaussmeter probe tip used. A sample coil centered in the magnetic field gap generated 7.2 N/A rather than the 8.0 N/A predicted by the FEA results, a difference of 10% which may be attributable to FEA errors and a coil winding less dense than expected.

5 POSITION SENSING

Position is sensed by three LEDs on the flotor and three planar position sensitive photodiodes on the outer stator. These provide six independent variables (x and y on each sensor) which can be transformed into the position and orientation of the flotor. The three sensors are mutually orthogonal to maximize position accuracy and simplify the geometric calculations.

Since the largest commercially available position sensitive photodiodes have an active area smaller than the range of motion of this device, direct sensing of the LEDs is not possible. Therefore, lenses are used to demagnify the motion of each LED by the ratio of 2.5:1. Wide angle LEDs will be used to insure that light from the LED always fills the lens.

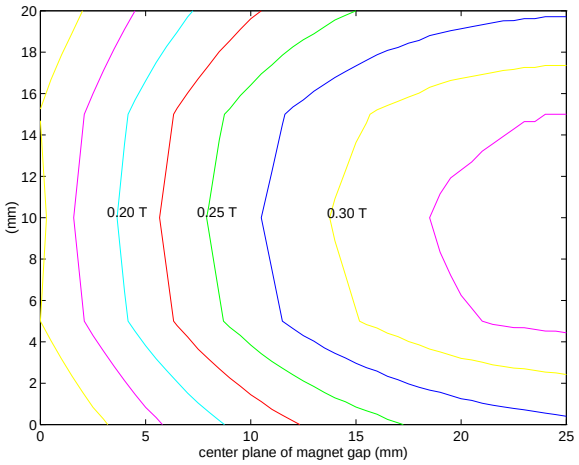

Figure 7: Measurement of Magnetic Field in Air Gap

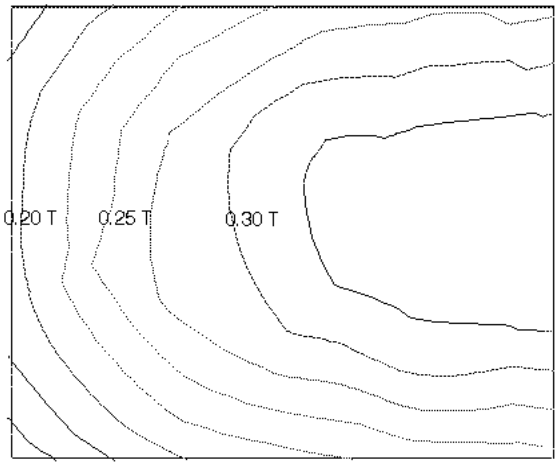

Figure 8: FEA Predicted Magnetic Field in Air Gap

As shown in Fig. 9, the coordinate frames required for the forward kinematics are the stator frame $\{s\}$, the flotor frame $\{f\}$ (which is coincident with the stator frame when the flotor is at its home position), and a frame at each lens $\{a\}$, $\{b\}$, and $\{c\}$. The forward kinematics are computed by first finding the position of the LED in its corresponding lens frame with respect to the transformation matrix ${}^s_f T$, which describes the flotor's motion. With the constant vector ${}^f A$ (the location of LED a with respect to the flotor frame) and the constant transformation matrix ${}^a_s T$, this is given by

$$ {}^a A = {}^a_s T \, {}^s_f T \, {}^f A.$$

The light source is imaged on the sensor at a point given by

$$\begin{bmatrix} s_{a,x} \\ s_{a,y} \end{bmatrix} = \left(\frac{-l_z}{\{{}^a A\}_z} \right) \begin{bmatrix} \{{}^a A\}_x \\ \{{}^a A\}_y \end{bmatrix},$$

where l_z is the distance from the lens to the sensor.

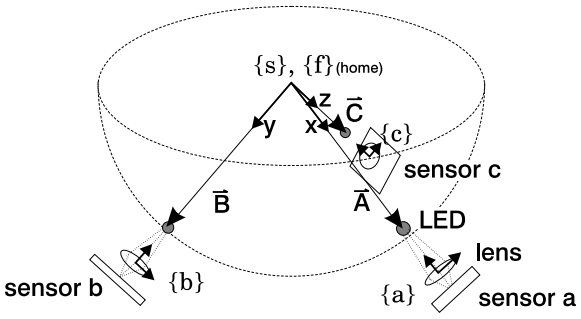

Figure 9: Stator, Flotor, and Sensor Frames for Position Sensing

For the Jacobian to be square, the forward kinematics should be a function of six independent variables, not a rotation matrix. The variables used are $\{n_1 \; n_2 \; \theta \; X \; Y \; Z\}$, where n_1 and n_2 represent the x and y components of a normalized rotation axis, θ the rotation angle about this axis, and X, Y, and Z the translational motion of the origin. Creating ${}^s_f T$ as a function of these six variables plus n_3 (the z component of the rotation axis) and computing $s_{a,x}$ and $s_{a,y}$ from the equations above gives:

$$s_{a,x} = \frac{l_z l_l [n_1 n_3 (1 - \cos\theta) - n_2 \sin\theta] + Z}{l_l [n_1^2 + (1 - n_1^2)\cos\theta] + X + l_z - l_t},$$

$$s_{a,y} = \frac{l_z l_l [n_1 n_2 (1 - \cos\theta) + n_3 \sin\theta] + Y}{l_l [n_1^2 + (1 - n_1^2)\cos\theta] + X + l_z - l_t},$$

where l_l is the distance from the origin to the lens and l_t the distance from the origin to the sensor. Similar computations for the other two sensors give:

$$s_{b,x} = \frac{l_z l_l [n_1 n_2 (1 - \cos\theta) - n_3 \sin\theta] + X}{l_l [n_2^2 + (1 - n_2^2)\cos\theta] + Y + l_z - l_t},$$

$$s_{b,y} = \frac{l_z l_l [n_2 n_3 (1 - \cos\theta) + n_1 \sin\theta] + Z}{l_l [n_2^2 + (1 - n_2^2)\cos\theta] + Y + l_z - l_t},$$

$$s_{c,x} = \frac{l_z l_l [n_2 n_3 (1 - \cos\theta) - n_1 \sin\theta] + Y}{l_l [n_3^2 + (1 - n_3^2)\cos\theta] + Z + l_z - l_t},$$

$$s_{c,y} = \frac{l_z l_l [n_1 n_3 (1 - \cos\theta) + n_2 \sin\theta] + X}{l_l [n_3^2 + (1 - n_3^2)\cos\theta] + Z + l_z - l_t}.$$

Once these formulas are determined, computing the Jacobian symbolically is straightforward, although the resulting formulas are somewhat complicated. Once the Jacobian $\mathbf{J}$ is available, the transformation from sensor data to flotor displacement vector can be done using a modified Newton-Raphson method in six dimensions, since the forward kinematics from flotor position to sensor data is known analytically, but there is no closed-form solution to

the inverse kinematics, and a six-dimensional lookup table of flotor vector with respect to sensor data would be prohibitively large. Newton-Raphson uses the numerical inverse of the Jacobian to determine the next step of the iteration with the update rule

$$\mathbf{x^{(i+1)}} = \mathbf{x^{(i)}} + \mathbf{J^{-1}}[\mathbf{s} - \mathbf{f}(\mathbf{x^{(i)}})],$$

where $\mathbf{s}$ is a vector of the known sensor values and $\mathbf{f}(\mathbf{x^{(i)}})$ is the predicted sensor values for the previous estimate of the flotor location. The system implemented for the haptic device cannot calculate the inverse Jacobian at run-time, since this is too computationally expensive, but instead will pick one out of a 3^6 entry lookup table which can be calculated beforehand. This slows the convergence slightly in terms of number of iterations required, but greatly increases the overall speed.

Since each photodiode output is not linear with respect to position to the accuracy required, tests have been performed to see if the nonlinearity is a repeatable phenomenon which could then be factored out at run-time. These tests were performed by first mapping out the relationship between true light position and reported sensor position and using this data to create a lookup table. The light was then qplaced at random known points around the sensor, and the results of the table lookup were found to be in close agreement with the known light positions. The lookup tables generated during these tests will be used at run-time to convert from each sensor output (in V) to true light position (in mm), which can then be used by the inverse kinematics routine. In addition, during these tests, the short-term repeatability of the sensor was shown to be on the order of ± 3 μm, and could be further improved by using low-noise components in the sensor circuitry. The cartesian position resolution of the flotor can then be calculated to within 3 μm.

In a software simulation, the iterative method was found to solve the flotor displacement vector $\mathbf{x}$ from simulated sensor data $\mathbf{s}$ in an average of approximately 700 floating-point operations. By performing the necessary calculations on our available digital signal processor in the realtime control system, a feedback sampling rate of at least 1000 Hz can be obtained. Additional software has been written to automate the creation of lookup tables for the sensor linearization.

6 CONCLUSIONS AND FURTHER WORK

The design of the new haptic interface device is complete and parts fabrication is currently underway. Preliminary testing of the actuator magnet, coil assemblies and position sensitive photodiodes indicates that the performance goals set for the device can be realized.

Following completion of the device and its control system, we plan to integrate the haptic interface with realtime dynamic simulation software. Development of realtime, interactive three-dimensional physical simulation has been done by Baraff *et al* [8, 9]. Such a fast simulation system, with a synchronized graphical display, would effectively demonstrate the high performance haptic interaction capabilities of this device.

ACKNOWLEDGEMENTS

This work was supported by NSF grant IRI-940869, the Carnegie Mellon University Robotics Ph.D Program, and the Engineering Design Research Center, a NSF Engineering Research Center. The assistance of Todd Okimoto in measuring the magnetic field of the actuator assembly is acknowledged.

References

[1] F. Brooks, Jr., M. Ouh-Young, J. J. Batter, and P. Kilpatrick, "Project GROPE—haptic displays for scientific visualization," *Computer Graphics*, vol. 24(4), pp. 177–185, August, 1990.

[2] M. L. Agronin, "The design of a nine-string six-degree-of-freedom force-feedback joystick for telemanipulation," in *Proc. NASA Workshop on Space Telerobotics*, pp. 341–348, 1987.

[3] M. D. Bryfogle, C. C. Nguyen, S. S. Antrazi, and P. C. Chiou, "Kinematics and control of a fully parallel force-reflecting hand controller for manipulator teleoperation," *Journal of Robot Systems*, vol. 10, no. 5, pp. 745–766, 1993.

[4] T. Massie and K. Salisbury, "The phantom haptic interface: A device for probing virtual objects," in *Proceedings of the ASME Winter Annual Meeting, Symposium on Haptic Interfaces for Virtual Environment and Teleoperator Systems*, (Chicago, Illinois), November 1994.

[5] R. L. Hollis and S. E. Salcudean, "Lorentz levitation technology: a new approach to fine motion robotics, teleoperation, haptic interfaces, and vibration isolation," in *Proc. 6th Int'l Symposium on Robotics Research*, (Hidden Valley, PA), October 2-5 1993.

[6] P. J. Berkelman, R. L. Hollis, and S. E. Salcudean, "Interacting with virtual environments using a magnetic levitation haptic interface," in *Int'l Conf. on Intelligent Robots and Systems*, (Pittsburgh), pp. 2296–2301, August 1995.

[7] R. L. Hollis, S. Salcudean, and A. P. Allan, "A six degree-of-freedom magnetically levitated variable compliance fine motion wrist: design, modeling, and control," *IEEE Transactions on Robotics and Automation*, vol. 7, pp. 320–332, June 1991.

[8] D. Baraff, "Issues in computing contact forces for non-penetrating rigid bodies," *Algorithmica*, vol. 10, pp. 292–352, 1993.

[9] D. Baraff and A. Witkin, "Dynamic simulation of non-penetrating flexible bodies," in *Computer Graphics (Proc. SIGGRAPH)*, vol. 26, pp. 303–308, ACM, July 1992.